Understanding the rapid reoxidation process and the electrical properties of Spark Plasma sintered pyrochlores

Emerson Luiz dos Santos Veiga, Héctor Beltrán-Mir, Héctor Beltrán-Mir, Sébastien Fourcade, U-Chan Chung, Catherine Elissalde, Fabrice Mauvy, Eloísa Cordoncillo

▶ **To cite this version:**

Emerson Luiz dos Santos Veiga, Héctor Beltrán-Mir, Héctor Beltrán-Mir, Sébastien Fourcade, U-Chan Chung, et al.. Understanding the rapid reoxidation process and the electrical properties of Spark Plasma sintered pyrochlores. Journal of the European Ceramic Society, 2024, 44 (6), pp.4130-4140. 10.1016/j.jeurceramsoc.2023.12.070 . hal-04432472

HAL Id: hal-04432472
https://hal.science/hal-04432472

Submitted on 1 Feb 2024

HAL is a multi-disciplinary open access archive for the deposit and dissemination of scientific research documents, whether they are published or not. The documents may come from teaching and research institutions in France or abroad, or from public or private research centers.

L'archive ouverte pluridisciplinaire **HAL**, est destinée au dépôt et à la diffusion de documents scientifiques de niveau recherche, publiés ou non, émanant des établissements d'enseignement et de recherche français ou étrangers, des laboratoires publics ou privés.

Journal of the European Ceramic Society xxx (xxxx) xxx

Contents lists available at ScienceDirect

Journal of the European Ceramic Society

journal homepage: www.elsevier.com/locate/jeurceramsoc

Understanding the rapid reoxidation process and the electrical properties of Spark Plasma sintered pyrochlores

Emerson Luiz dos Santos Veiga [a,*], Héctor Beltrán-Mir [a,*], Sébastien Fourcade [b], U.-Chan Chung [b], Dominique Michau [b], Catherine Elissalde [b], Fabrice Mauvy [b], Eloísa Cordoncillo [a,*]

[a] Departamento de Química Inorgánica y Orgánica, Universitat Jaume I, 12071 Castellón de la Plana, Spain
[b] CNRS, Université de Bordeaux, ICMCB, 87 avenue du Dr. A. Schweitzer, F-33608 Pessac, France

ARTICLE INFO

Keywords:
Spark plasma sintering
Pyrochlore
Reoxidation
Electrical properties
Impedance spectroscopy

ABSTRACT

Pyrochlore structures with composition $Pr_{2-x}Sm_xZr_2O_7$ (x = 0, 1, and 2) were synthetized and studied. Spark Plasma Sintering (SPS) was employed to produce ceramics with over 95% of relative density. The reoxidation behavior and the influence of the sintering process on the electrical properties were studied by Electrochemical Impedance Spectroscopy. The overall conductivity of the materials is higher for the samples with Pr, while the introduction of Sm induced an additional electrical contribution. The reoxidation of the samples presented fast kinetics and increased conductivity, particularly in the $PrSmZr_2O_7$ (PSZO) sample. PSZO also exhibits a total conductivity comparable to that of the reference materials used as ionically conductive solid electrolytes. The prepared ceramics, especially the PSZO sample, demonstrate excellent relative density, good conductivity, and fast oxidation, holding promise for applications such as Solid Oxide Fuel Cells, gas sensors, and clean energy technologies that require thermal and physical stability, as well as rapid oxidation-reduction processes.

1. Introduction

Ceramic materials have long been recognized for their exceptional thermal and chemical stability, making them attractive for a wide range of applications [1,2]. Advancements in ceramic processing techniques have enabled the development of materials with tailored properties, opening up opportunities for their utilization in electronic devices [3]. Many of these devices heavily rely on redox reactions occurring at the material-electrolyte interfaces.

One notable example is the application of ceramic materials in Solid Oxide Fuel Cells (SOFCs). In the SOFC technology, a fuel is oxidized at the anode side, releasing electrons, while O^{2-} oxygen ions transported through the electrolyte migrate from the cathode side to the fuel electrode, where they react with the fuel, completing the electrochemical process [4–7]. To maintain optimal cell performance, a constant and fast supply of oxygen ions at the electrolyte-electrode interfaces is crucial, requiring precise control of the cell architecture.

Besides SOFCs, ceramic materials also integrate gas sensors, which enable the detection and quantification of specific gases. These sensors operate based on redox reactions occurring at the material's surface, generating measurable electrical signals. The oxygen exchange process plays a key role in ensuring the sensor's sensitivity, selectivity, and response time, thereby optimizing its performance [8–12].

Moreover, ceramic materials are employed in catalytic converters found in automotive exhaust systems. These ceramics serve as catalyst supports, facilitating the oxidation and reduction reactions of harmful exhaust gases. The reoxidation of the ceramic support is vital to maintaining its catalytic activity, enabling efficient conversion of pollutants into less harmful substances, such as carbon monoxide (CO), nitrogen oxides (NO_x), and hydrocarbons [13–16].

By studying and understanding the oxygen exchange process in ceramics, researchers can enhance the performance, stability, and durability of electronic devices, including SOFCs, gas sensors, and catalytic converters, for example. This knowledge allows the optimization of the material properties and operating conditions, leading to progresses in energy conversion efficiency, gas sensing capabilities, and environmental sustainability.

In this context, pyrochlore structures with rare-earth cations stand out as a class of ceramics with unique chemical and physical properties. Indeed, pyrochlore materials exhibit a highly ordered crystal structure,

* Corresponding authors.
E-mail addresses: edossant@uji.es (E.L. dos Santos Veiga), mir@uji.es (H. Beltrán-Mir), cordonci@uji.es (E. Cordoncillo).

with general formula $A_2B_2O_7$, where the A-site cations are larger and typically have a lower oxidation state, while the B-site cations are smaller and have a higher oxidation state. The A-site can be occupied by rare-earth ions and is located in the center of the oxygen octahedra. The B-site, normally occupied by transition metals cations reside within the oxygen octahedra. Moreover, the inherent additional anion vacancy present in site 8a resides in the tetrahedral interstice between adjacent B-site cations. The pyrochlore coordination environment provides opportunities for various cationic configurations and different oxidation states [17–19].

The structural arrangement together with the capacity of incorporating a wide range of ions, can promote remarkable chemical stability and resistance to structural degradation, making the pyrochlores well-suited for high temperature applications such as solid oxide fuel cells [20–23], gas sensors [24–26], and catalytic converters [27,28], especially when ions that can exhibit different oxidation states are present, such as Pr(III/IV) and Ce(III/IV) [29–31]. Additionally, their low thermal conductivity [32,33], low dielectric losses [34,35], and ionic conductivity [36–38] make pyrochlore ceramics promising candidates for advanced energy conversion and storage systems.

To achieve the desired properties of a pyrochlore material, the processing step is crucial, especially with the goal of maintaining this crystalline structure while obtaining a dense ceramic. Conventional sintering of these materials does not allow to reach the expected density ($\geq$95%) [39]. On the other hand, new unconventional sintering techniques such as Flash Sintering [40], Cold Sintering [41] or Spark Plasma Sintering (SPS) [42] have proven their efficiency to densify functional ceramics. Among these techniques, SPS combines the simultaneous action of uniaxial pressure and pulsed electrical current, providing efficient heat transfer to the material and fast sintering kinetics [43–46]. The SPS process can lead to significant improvements in the relative density, which may impact in the properties such as mechanical strength, electrical conductivity, and chemical stability of pyrochlore structures. The low O_2 partial pressure environment used in SPS can induce reduction of chemical species and thus a change in the properties of these materials making them even more attractive for the applications previously mentioned.

In this context, the present work investigates the reoxidation process of pyrochlore materials with formula $Pr_{2-x}Sm_xZr_2O_7$ (x = 0, 1, and 2) sintered by Spark Plasma by analyzing how the electrical behavior of the different prepared compositions is affected in different atmospheres. By gaining insights into the reoxidation behavior and understanding the impact of sintering on pyrochlore ceramics, this work contributes to advancing the knowledge and potential applications of these materials.

2. EXPERIMENTAL SECTION

Three different nominal compositions of $Pr_{2-x}Sm_xZr_2O_7$, with x = 0, 1, and 2, named as PZO, PSZO, and SZO, respectively, were prepared by the solvothermal synthesis method. This synthesis method offers several advantages over the traditional solid-state method. For instance, it allows the production of nano-sized particles, it is relatively simple and cost-effective. Furthermore, it provides better control over the reaction stoichiometry, and it is easily reproducible [31].

The precursors used were $Pr(CH_3COO)_3{\cdot}x\ H_2O$ (Strem Chemicals, 99.9%), $Sm(CH_3COO)_3{\cdot}x\ H_2O$ (Sigma–Aldrich, 99.9%), and $ZrOCl_2{\cdot}8\ H_2O$ (Alfa Aesar, 98%). The precursors of zirconium, praseodymium, and samarium were dissolved in 30 mL of distilled water. Subsequently, the pH of the solution was adjusted close to 10 by adding ammonia solution (Scharlab, 32% w/w). The resulting suspension was vigorously stirred for 10 min and then transferred to a Teflon-lined vessel with a capacity of 125 mL. The total volume of the solution was approximately 50 mL. Next, the Teflon vessel was placed in a digestion bomb and heated in an oven at 180 °C for 24 h. Afterward, the system was allowed to cool, and each suspension was dried at 100 °C for 24 h. The products were grounded and fired at 1200 °C for 2 h with a heating ramp of 5 °C min^{-1}.

The resulting powders were sintered into pellets by Spark Plasma Sintering (SPS) using a SYNTEX.INC, Dr. Sinter 515 S apparatus. SPS was conducted under dynamic primary vacuum conditions (starting between pressures of 7 Pa–10 Pa and stabilizing at 7 Pa–8 Pa) to prevent oxidation of the graphite, and at a temperature of 1350 °C. Short dwell time (5 min) and standard heating rates (50 °C - 100 °C min^{-1}) were used to improve the relative density and reduce the grain growth. The uniaxial pressure (100 MPa) was applied starting from ambient temperature and maintained throughout the heating process until the sintering temperature dwell was completed. The pressure was then released during the cooling step until the temperature reached T $\leq$ 600 °C. Graphite molds and punches were used, and the interior of the mold was covered with graphite foil ensuring a good electrical contact within the parts.

X-ray Diffraction (XRD) analysis, a Bruker-AX D8-Advance X-ray diffractometer with Cu-Kα radiation was used to identify the phases present in each composition. The data were collected at room temperature within the range of 10° $\leq 2\theta \leq$70°, with a step size of 0.03° and a counting time of 3 s for each step. X-ray diffraction was performed using the grounded powder of the sintered pellet. To obtain more detailed information regarding the cell parameters and density, the Rietveld Refinement (RR) method was applied using the freely available software GSAS-II [47].

The experimental density of the sintered pellets was determined using the Archimedes method [48]. The procedure was repeated multiple times per sample to ensure the reliability and reproducibility of the results. The calculation of the relative density of the samples in % was obtained using the theoretical density obtained by the RR and the experimental density.

The microstructure and morphology of cross-section of the pellets were analyzed using a JEOL 7001 Field-Emission Scanning Electron Microscope (FE-SEM) with an acceleration voltage of 15 kV. The pellet fracture surfaces were polished, followed by a 10-minute chemical etching with a 5% hydrofluoric acid solution (Sigma-Aldrich, 48%). Subsequently, the pellets were gold-sputtered for surface analysis.

In order to investigate the electrical behavior of the prepared materials, Electrochemical Impedance Spectroscopy (EIS) was employed. To ensure optimal electrode contact, platinum electrodes were sputtered onto opposing surfaces of the pellets using Physical Vapor Deposition (PVD). PVD procedure can be performed at room temperature, and the use of platinum avoids the need for post-thermal treatment that may result in sample reoxidation. Furthermore, platinum electrodes remain stable at temperatures up to 800 °C, making them suitable for the intended experiments [44].

The samples with the deposited electrodes were positioned in a conductivity jig, placed in a quartz chamber to enable and control the gas flow, and EIS measurements were carried out using an Agilent 4294A analyzer (Madrid, Spain). The EIS measurements were conducted within a frequency range of 40 Hz to 13 MHz, applying an AC voltage of 0.1 V, under different atmospheric conditions including dry Argon, Air, and N_2-H_2 5–95. To account for the overall pellet geometry, the impedance data were appropriately corrected.

3. Results and discussion

3.1. Structural and morphological evaluation

The pellets prepared using SPS were grounded and analyzed by XRD. Single-phase ordered pyrochlore structures with an *Fd-3 m* space group were obtained for all compositions, as shown in Fig. 1a. The presence of the ordered pyrochlore phase is indicated by the emergence of superstructure peaks at approximately °2θ°≈ °14° (111) and 37° (331), marked in this figure with arrows. These peaks arise from the necessary rearrangement required to transform a fluorite into a pyrochlore structure, including radiation scattering of cations A and B, displacement of oxygen from its ideal position, and the creation of oxygen vacancies [49,

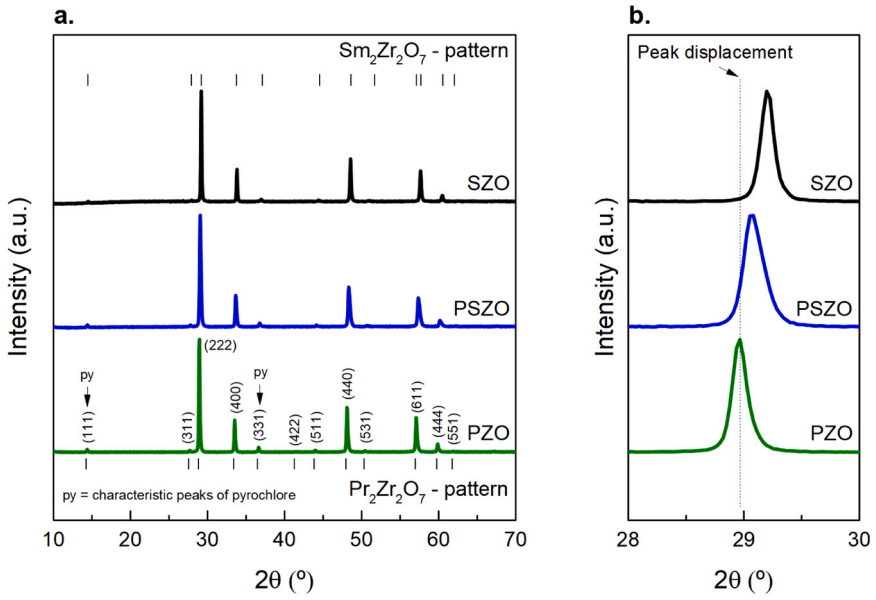

Fig. 1. (a) XRD patterns of the grounded SPS pellets of PZO, PSZO, and SZO materials. Crystallographic cards of the reference phases $Pr_2Zr_2O_7$ (JCPDS – ICDD 19–1021) and $Sm_2Zr_2O_7$ (JCPDS – ICDD 24–1012) are included. (b) Displacement of the (222) diffraction peak for the compositions prepared.

50].

Fig. 1b presents an enlarged view of the peak corresponding to the (111) crystalline plane. This enlargement allows for a clearer observation of the peak displacement towards higher angles in 2θ, which can be assigned to the difference in ionic radii between Pr(III) and Sm(III). In octahedral coordination, the ionic radii of Pr(III) and Sm(III) are equal to 112.6 pm and 107.9 pm, respectively [51]. This observation is in accordance with Bragg's Law, $n°\lambda\theta = 2d°\cos\theta$.

To detail the structural parameters of each composition, the Rietveld Refinement Method (RR) was employed. The summarized data for all calculations can be found in Table 1. A relevant refinement can be obtained by examining quality parameters that measure the discrepancy between the experimental data and the theoretically calculated values from the refined model, such as the χ^2 parameter, which is ideally close to unity, and the RF^2 parameter, preferably with values below 5% [52, 53].Taking all these factors into consideration, a good agreement between the observed and calculated profile patterns was achieved for all compositions (see Fig. S1).

The data obtained from RR measurements indicate a decrease in the lattice parameter *"a"* and, consequently, a reduction in the unit cell volume as the concentration of Sm increases in the pyrochlore structure. The site occupancy variables for the PZO and SZO samples were fixed based on the nominal stoichiometry used during preparation. In the case of the PSZO sample, these values suggest a slightly higher concentration of Sm. However, considering the uncertainty represented by the numbers in parentheses, it can be concluded that the Pr/Sm ratio in this sample is close to 1.

In the pyrochlore structure, there exists a single positional parameter referred to as the oxygen *"x"* parameter, which typically ranges from 0.309 to 0.355. This parameter specifically relates to the oxygen atoms located at the 48 f (x, 1/8, 1/8) site and describes their displacement within the tetrahedral interstices. On average, the oxygen atoms exhibit a displacement away from the center of the interstice towards the corners of the tetrahedron, although they do not reach the end points [49, 54]. Among all the samples analyzed, the PSZO composition displays the *x* value that is closest to the upper limit of 0.355. This observation suggests a higher degree of disorder for this particular composition. The higher degree of disorder may result in a greater number of mobile oxygen ions, potentially enhancing the ionic conductivity of the material [55,56].

SEM micrographs of the polished and etched cross section of the pellets prepared using SPS reveal distinct features depending on the sample composition, as can be seen in Fig. 2. In the case of the PZO sample, small grains ranging from approximately 50 to 200 nm are observed. However, for the other two samples containing Sm, much smaller grains are evident, making it difficult to estimate the average grain size.

The relative density of all pellets was determined by comparing the experimental density obtained using Archimedes' principle with the theoretical density derived from RR calculations. The results indicate that the relative density for all samples fall within the range of 95 to 96%, highlighting the high effectiveness of SPS as a technique for producing dense ceramics.

Table 1
Cell parameters and theorical densities were obtained by Rietveld Refinement.

	$Pr_2Zr_2O_7$	$PrSmZr_2O_7$	$Sm_2Zr_2O_7$
Refinement quality parameters			
χ^2	1.47	1.89	1.43
R_F^2 (%)	2.93	3.92	4.48
Structural parameters			
Cell length (Å)	10.71(1)	10.65(2)	10.61(1)
Cell volume ($Å^3$)	1228.66(1)	1206.31(2)	1193.30(1)
Theoretical density ($g\ cm^{-3}$)	6.23(1)	6.48(2)	6.63(1)
Site occupancy and positional parameter "x"			
A (Pr)	1	0.48(2)	-
A (Sm)	-	0.52(2)	1
B (Zr)	1	1	1
O (48 f)	1	1	1
O' (8b)	1	1	1
x (O 48 f)	0.327(1)	0.332(2)	0.330(1)

3.2. Electrical measurements under argon

Due to the low oxygen partial pressure during SPS, the materials undergo partial reduction during the sintering. The electrical measurements by EIS were initially conducted in an inert atmosphere of argon to prevent oxidation of the materials and to better understand the electrical response post-sintering.

Fig. 3 shows a typical set of impedance measurements for the three compositions studied. In Fig. 3a, which illustrates the impedance

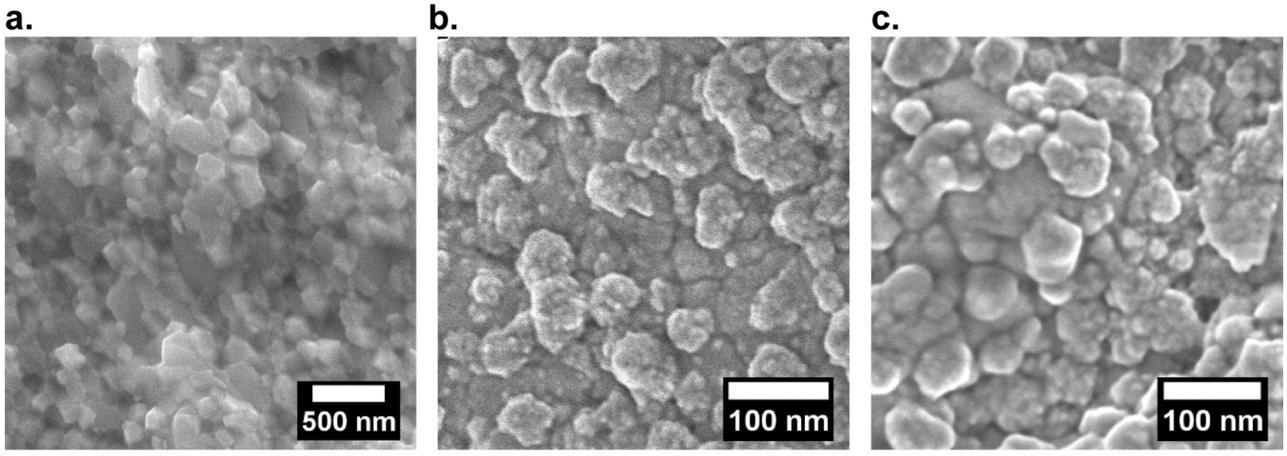

Fig. 2. Micrographs of the polished and etched cross section of the pellets after SPS: (a) PZO, (b) PSZO, and (c) SZO.

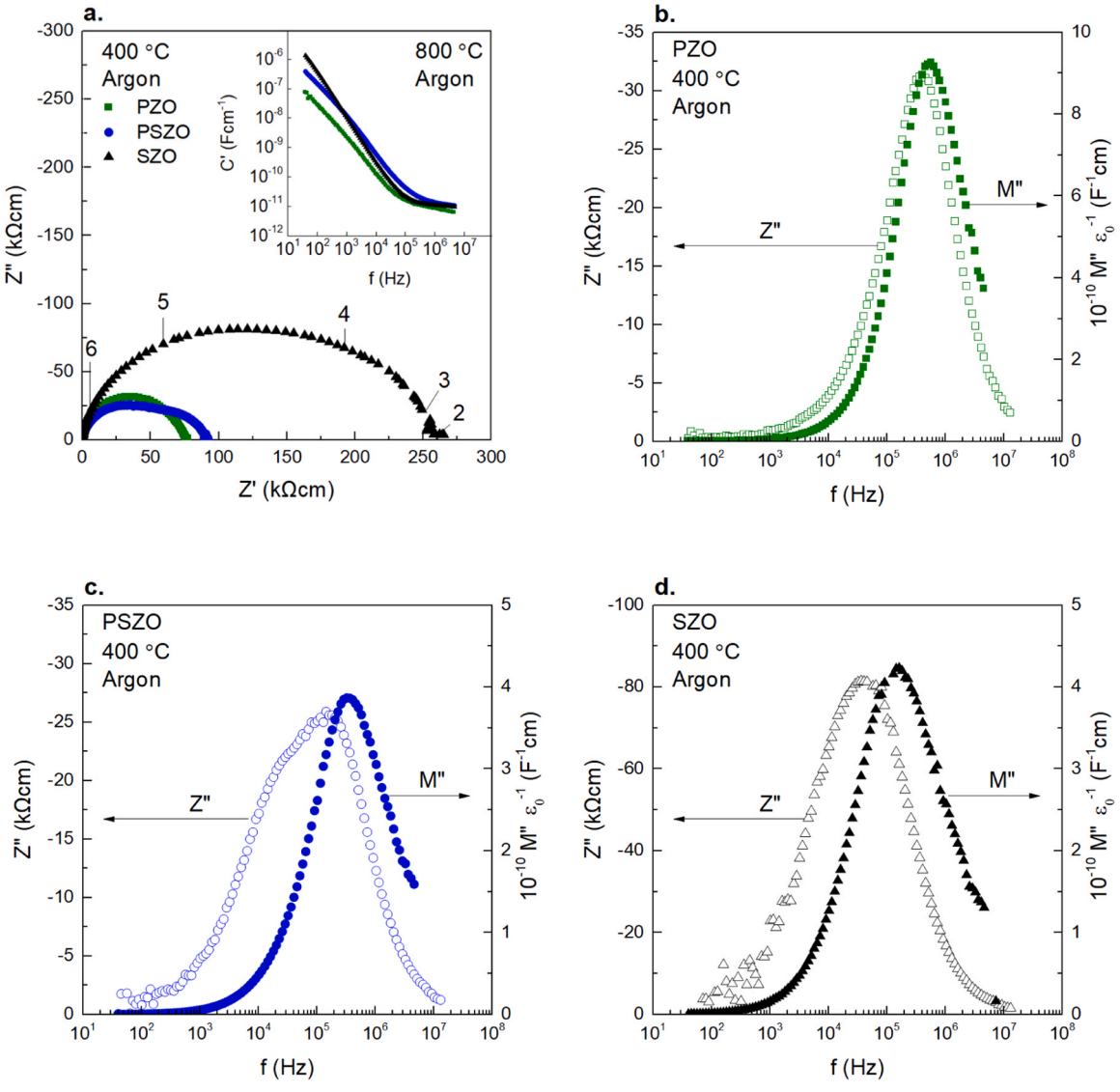

Fig. 3. (a) Impedance complex plane plots at 400 °C and the inserted *log C'/log f* plots at 800 °C for all samples. *Z"/M"* spectroscopy plots for (b) PZO, (c) PSZO, and (d) SZO at 400 °C. All IS measurements were taken in argon.

complex plane plots, also known as Nyquist plots (-Im(Z) versus *Re(Z), -Z'' versus Z'*), at 400 °C for all ceramics. One can observe an evident broad, depressed semi-circular arc for the SZO and PSZO samples suggesting the existence of multiple RC (resistance-capacitance) elements associated in series. However, the PZO sample exhibits a single and almost symmetric semi-circular arc, which can be associated to a single resistance of the sample bulk. At this temperature, the total resistance of each sample, obtained from the intercept of the arc on the *Z'* axis, are approximately 260 kΩ cm for SZO, 90 kΩ cm for PSZO, and 75 kΩ cm for PZO.

The log *C'/log f* plots inserted in Fig. 3a reveal the presence of a frequency-independent plateau at high-frequencies associated to the bulk capacitance for all samples, with capacitance values around 8×10^{-12} F cm^{-1}. It is important to mention that other plateau at low-frequencies, corresponding to grain boundary capacitance, is not observed and, consequently, the arc's asymmetry cause in the impedance complex plane plots for the SZO and PSZO samples is unclear, indicating the possible existence of distinct RC components with similar capacitances.

At low frequencies, *C'* increases to values ranging from approximately 10^{-7} to 10^{-6} F cm^{-1}, depending on the composition. These values are typical of ion blocking at a sample–electrode interface. Generally, at high temperatures, the capacitance of low-frequency ionic conductors surpasses values of 10^{-6} F cm^{-1} [57].

To clarify the possible presence of two different RC elements in the samples, the *Z″/M″* spectroscopic plots are showed in Fig. 3 for the three prepared compositions at 400 °C. The PZO (Fig. 3b) clearly exhibits a single Debye peak in each spectrum, with approximately similar maximum frequencies. Considering that low *M″* diagrams are predominantly influenced by low capacitance bulk effects, the data presented in Fig. 3a, together with the associated capacitance inserted in this figure, suggests that the primary resistive component of the PZO sample corresponds to the bulk. Consequently, the PZO sample can be described by a simple single parallel RC element, where the total resistance, R, reflects the resistance of the grains. This observation indicates that the PZO is electrically homogeneous.

However, in the case of the PSZO sample (Fig. 3c) and the SZO sample (Fig. 3d), the *M″* and *Z″* peak maxima do not match at the same frequency maximum. Additionally, the *Z″* peak in both spectra exhibits a broader format than expected for an ideal Debye peak. This discrepancy further suggests a potential electrical inhomogeneity within the sample [58], which becomes more prominent as the Sm concentration increases. This effect can be induced by a combination of either a constriction grain boundary after the sintering process and possible inhomogeneous distribution of Sm(III) and Pr(III/IV) ions [58].

The total resistance of each sample was obtained from intercepts of the arc on the *Z'* axis of the impedance complex plane plots and are shown as total conductivity in Arrhenius format as function of temperature, as seen in Fig. 4. The impedance measurements at different temperatures were performed after the system reached steady state conditions. The activation energies are also shown beside each data set. The higher activation energy was found for the SZO sample (0.95 eV), followed by the PSZO (0.80 eV).

The PZO presented two activation energies: one in the temperature range of 250 °C to 450 °C, with a value of 0.77 eV, and the second at temperatures of 500 °C to 800 °C, which presented an activation energy of 0.48 eV. It was verified in previous studies that between 450 °C and 500 °C [39], the spontaneous reduction of praseodymium occurs. Therefore, it is possible that not all of the praseodymium ions were reduced after the SPS process. The PSZO sample probably also contains a mixture of Pr(III) and Pr(IV) ions, so the reduction of Pr(IV) is also expected, however, if present, this effect is not as evident for the PSZO sample as for PZO.

The PSZO sample exhibits a total conductivity comparable to that of the PZO sample at lower temperatures. However, at higher temperatures, its total conductivity becomes more similar to the SZO sample and

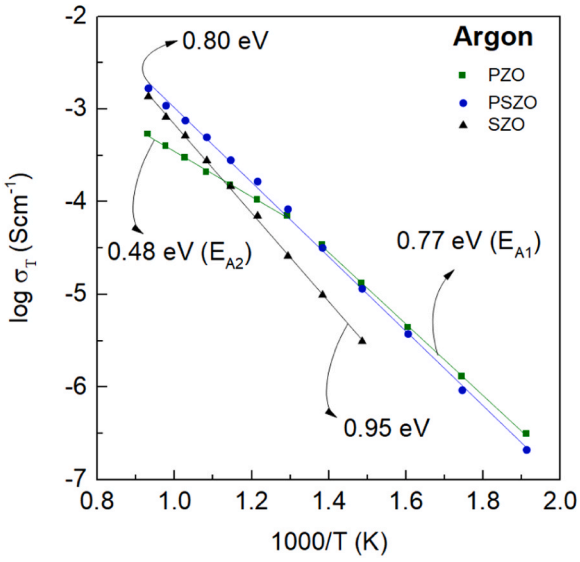

Fig. 4. Arrhenius plot of the overall conductivity in argon for all samples. The activation energy (eV), with errors in the range 0.02–0.05 eV, are shown beside each data set.

is even slightly higher, reaching approximately 1.7×10^{-3} S cm^{-1} at 800 °C. At this temperature, the total conductivities of SZO and PZO are 1.4×10^{-3} S cm^{-1} and 5.4×10^{-4} S cm^{-1}, respectively. The higher conductivity for the PSZO sample at higher temperatures may be associated with the disorder in the pyrochlore structure.

3.3. Study of the reoxidation process

To evaluate the in-situ oxidation kinetics, EIS measurements were performed at specific time intervals to track the oxidation process of each material based on its electrical response. The oxidation kinetics tests were performed at two different temperatures: 800 °C and 600 °C, using freshly prepared pellets, as illustrated in Fig. 5a and b, respectively. The experimental procedure involved stabilizing the temperature until the material reached a steady state, in accordance with the EIS measurements performed under inert atmosphere (argon). Then the atmosphere was switched to air, and the conductivity was monitored over time. The empty symbols in each figure represent the measurement in argon, and the filled symbols represent all measurements taken in air.

At both studied temperatures, the only sample that did not show significant changes in its conductivity throughout the entire testing period was the SZO sample. The ions present in this sample do not exhibit different oxidation states, suggesting that the conduction occurs manly by O^{2-} ions. Given that the sample remains unaffected by the variations in the oxygen partial pressure, pO_2, used in this experiment, it suggests that under these conditions this material is in the electrolytic domain, as it occurs in other ionic conductors, such as YSZ (Yttria-Stabilized Zirconia) under similar pO_2 conditions [58,59].

The PZO and PSZO samples exhibit distinct behavior compared to the SZO sample. When the atmosphere is changed from argon to air, both samples demonstrate an immediately substantial increase in conductivity, which stabilizes within approximately 30 min. Furthermore, lowering the test temperature from 800 °C to 600 °C, no significant reduction in the oxidation rate of the samples was observed. Consequently, it can be concluded that these samples display rapid oxidation kinetics.

The enhanced conductivity in an oxidizing atmosphere can be attributed to the absorption of oxygen on the surface of the material. This absorption process partially oxidizes the Pr(III) species to Pr(IV), reducing the number of available electrons for the formation of O^{2-} ions, leading to hole creation on oxygen (Eq. (1)). Consequently, the

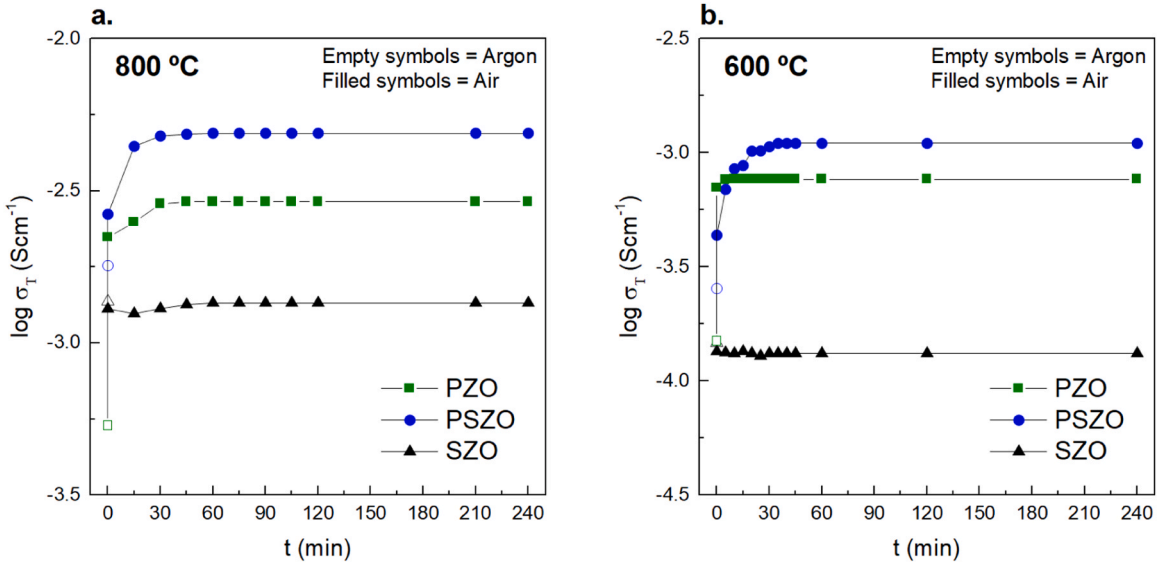

Fig. 5. Monitoring the reoxidation kinetics of the samples over time at temperatures of (a) 600 °C and (b) 800 °C through IS measurements when changing the atmosphere from argon (empty symbols) to air (filled symbols).

material's conductivity is improved, indicating a characteristic behavior of a *p*-type semiconductor. In oxide-ion-conducting solid electrolytes, as this is the case of the prepared samples, the electrolytic domain is restricted at high pO_2 due to the onset of p-type conduction [39,58–60].

$$\frac{1}{2}\ O_2 + V_o^{\bullet\bullet} \leftrightarrow O_o^x + 2h^{\bullet} \quad (1)$$

This explanation is consistent with the concentration of Pr in each sample. Although the PSZO sample exhibits higher final conductivity, possibly assigned to structural disorder as mentioned earlier, the PZO sample demonstrates a greater variation in conductivity when comparing the first measurement conducted in argon to the last measurement performed in air (after 240 min). Hence, as the concentration of Pr ions increases, a more substantial oxidation of Pr occurs, resulting in a greater generation of charge carriers (holes) and a higher difference in conductivity in the tested atmospheres.

To achieve a deeper understanding of the electrical behavior of the samples under oxidizing conditions, EIS measurements were conducted during cooling from 800 °C until room temperature in air. Fig. 6 illustrates a set of the EIS data collected at 400 °C for all the samples analyzed after oxidation.

In Fig. 6a, the impedance complex plane plots reveal a significant decrease in resistivity for the Pr-containing samples in comparison with the EIS measurements performed under argon (Fig. 3a), indicating the effect of the oxidation process. However, the overall conductivity for the SZO sample is almost the same to that observed in argon. The SZO sample continues to exhibit a broad, depressed arc, while the inset in this figure shows the impedance complex plane plot of the PZO sample, which demonstrates a single symmetrical semi-circular arc. On the other hand, the PSZO sample stands out by exhibiting two well-defined semi-circular arcs, suggesting the presence of two distinct RC elements. These elements were not clearly observable in the argon measurements discussed earlier (as shown in Fig. 3).

The presence of the two RC elements in series in the PSZO sample is also evident in the *log C'/log f* plots presented in Fig. 6b. At low frequencies, a frequency-independent plateau with a capacitance value of approximately 1×10^{-11} F cm^{-1} is observed, associated to the sample bulk. Additionally, a second plateau is observed at higher frequencies, characterized by a capacitance value of 4.5×10^{-10} F cm^{-1}, which can be attributed to the grain boundary. Comparing the *C'* values with the impedance data measured under argon shown in Fig. 3b, it is possible that a different oxidation process takes place for the bulk and the grain boundary when exposing the PSZO to an oxidizing atmosphere. This effect likely contributes to a more distinct separation between the two RC elements observed in the EIS measurements performed under air.

The Z''/M'' spectroscopic plots shown in Fig. 6c for the PZO at 400 °C display a single Debye peak in each spectrum, with approximately similar maximum frequencies. Therefore, similar to the same EIS measurements under argon, the total resistance of this sample is associated with the bulk. Its electrical response in air also can be represented by a single RC element.

In the case of the PSZO sample (Fig. 6d), a second peak is observed in the Z'' diagram, indicating the presence of an additional resistance associated with the grain boundary. Hence, in an oxidizing atmosphere, it is necessary to include a second element (R_2) to better describe the ionic transport behavior of the ceramic sample.

Lastly, in the case of SZO (Fig. 6e), the Z''/M'' spectroscopic plots exhibit the appearance of broad peaks with non-ideal Debye formats. The maximums of each peak do not coincide at the same frequency. As a result, this sample, like the EIS measurements under argon (Fig. 3d), remains electrically inhomogeneous under air.

The total conductivity when decreasing temperature in air is represented in Arrhenius format in Fig. 7a for all samples. As shown in this graph, similar to the observations in argon, the PZO sample displays two activation energies, with lower values in air, resulting from the oxidation of Pr(III) species after 500 °C, since now the EIS measurements are taken when cooling the system. Additionally, the PZO sample exhibits higher total conductivity in air than in argon (Fig. 4) across the entire temperature range studied. This increase is attributed to the generation of charge carriers in an oxidizing atmosphere. Since the Z''/M'' spectroscopic plots indicate that the PZO sample can be represented using a single RC element (Fig. 6c), the increase in conductivity is related to the ionic response of the bulk.

In contrast, the SZO sample shows no significant change in conductivity across the temperature range after switching from argon to air and is less conductive than PZO and PSZO over the entire temperature range, presenting the same activation energy, 0.95 eV.

The case of the PSZO sample is particularly interesting. Indeed, this sample presents the highest conductivities in the temperature range from 500 °C to 800 °C. As seen in Fig. 6, the addition of a second RC element is necessary to accurately describe the electrical response of this ceramic sample. Consequently, it becomes possible to separate the contributions of the bulk and the grain boundary to the overall conductivity. The contributions of each region of the sample in air, as well

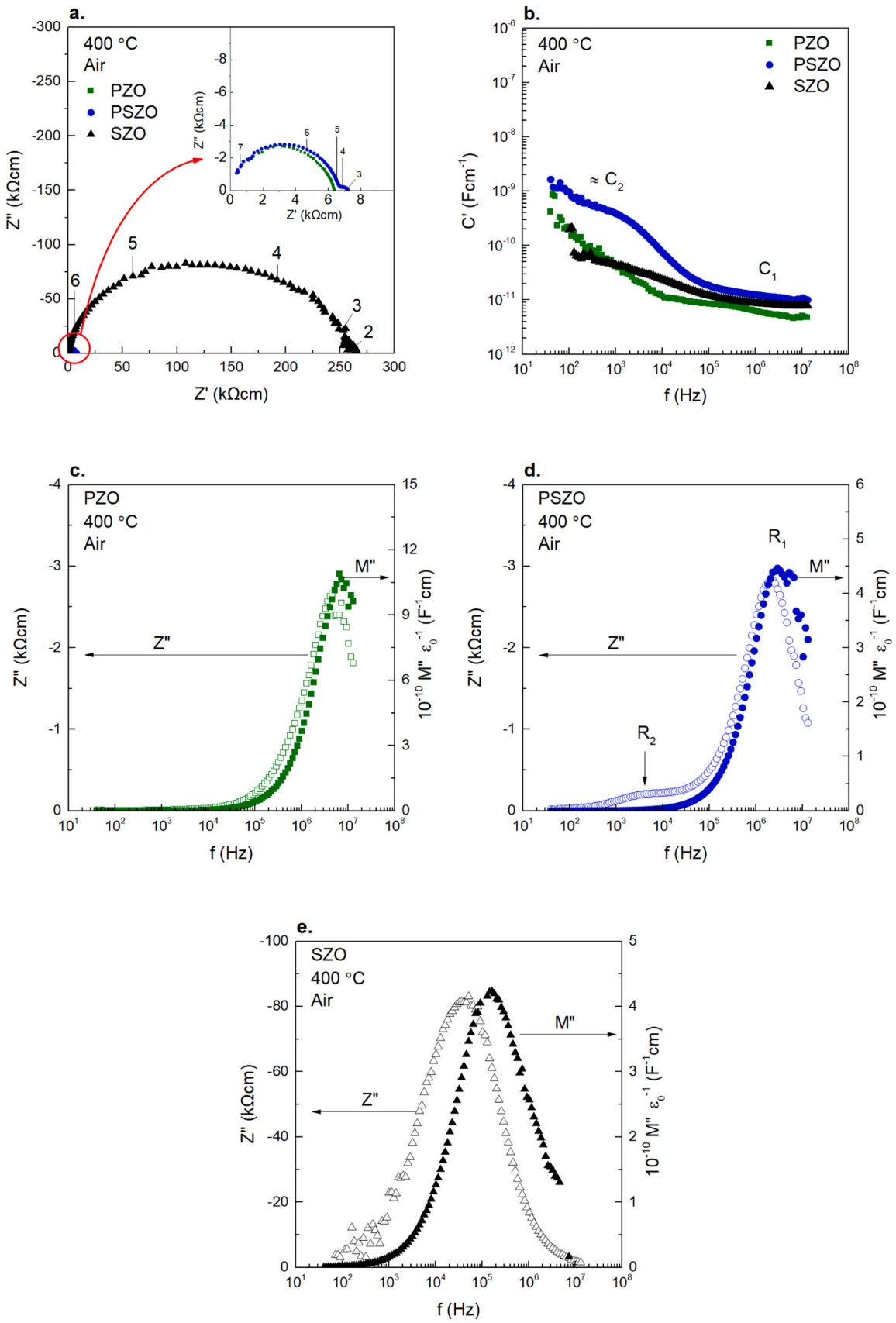

Fig. 6. (a) Impedance complex plane plots at 400 °C and 600 °C (inserted) for all samples. (b) *log C'/log f* plots at 400 °C. *Z''/M''* spectroscopy plots for (c) PZO, (d) PSZO, and (e) SZO at 400 °C. All IS measurements were taken in air.

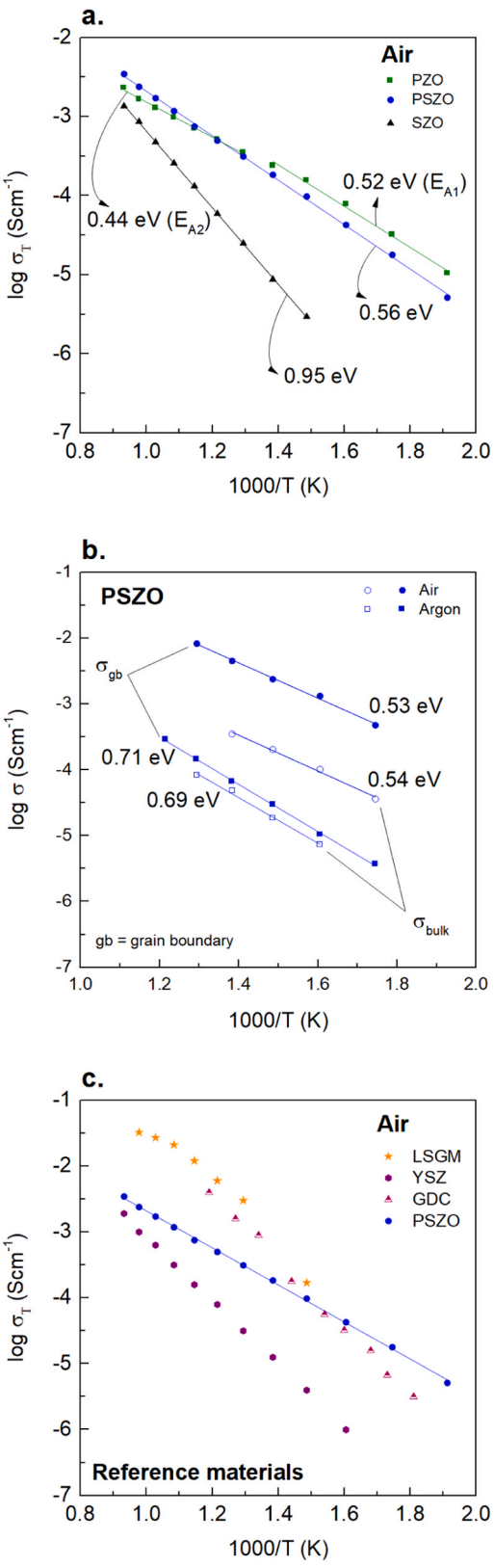

Fig. 7. (a) Arrhenius plot of the overall conductivity in air for all samples. (b) Bulk and grain boundary conductivities extracted by the *Z"/M"* spectroscopic plots for the PSZO sample in argon and air. (c) PSZO overall conductivity in air compared to reference ion-oxide solid electrolytes materials. The activation energy (eV), with errors in the range 0.02–0.05 eV, are shown beside each data set.

as in argon (inserted for comparison purposes), are shown in Fig. 7b. From this figure it can be observed a bulk conductivity increase under air, but the most significant conductivity increase occurs at the grain boundary and, therefore, the sample oxidation process predominantly takes place at the grain boundaries.

As PSZO compound presented the highest conductivity at high temperatures, Fig. 7c shows a comparison between this sample and reference materials commonly used as solid electrolytes for SOFCs. These reference materials exhibit favorable characteristics such as good ionic conductivity and stability at high temperatures. The conductivity of PSZO surpasses that of YSZ [61] in the whole temperature range. Additionally, PSZO exhibits comparable conductivity to LSGM (Lanthanum Strontium Gallate Magnesite) [46] and CDC (Gadolinium-Doped Ceria) [62] at temperatures below 500 °C. Consequently, this material seems to be promising for applications in fuel cells and other energy-related technologies.

To assess the stability of materials in a reducing atmosphere, EIS measurements were performed by gradually cooling the system from 800 °C to 300 °C in the presence of H_2. The overall conductivity of each material under these conditions is presented in Fig. 8. This figure also includes the overall conductivity curves previously demonstrated under argon and air for the purpose of comparison.

In Fig. 8a, the conductivity of the PZO sample exhibits a decrease throughout the temperature range studied when exposed to a reducing atmosphere. This decrease can be attributed to the reduction of Pr(IV) species, which results in a reduction in the number of charge carriers. Notably, the conductivity curve in reducing atmosphere (N_2/H_2 mixture) displays a single activation energy value of 0.82 eV, unlike the curves observed in argon and air. This discrepancy arises from the complete reduction of all Pr ions in H_2. Additionally, it can be inferred that not all of the Pr ions undergoes reduction after the SPS process, as evidenced by the lower conductivities observed in H_2 compared to EIS measurements in argon.

The decrease in total conductivity when exposed to H_2 is less pronounced in the PSZO sample compared to the PZO sample. The conductivity curves of PSZO in H_2 and in argon exhibit similar activation energies of 0.81 eV and 0.80 eV, respectively. This similarity in conductivity suggests that, due to the lower concentration of Pr in the PSZO sample compared to PZO, almost all ions undergo reduction following the SPS process.

Finally, the total conductivity curve of the SZO sample under H_2 exhibited no significant variations when compared to the curves obtained in both argon and air. This observation confirms that the SZO material does not undergo oxidation or reduction processes under the tested conditions.

Therefore, overall, the samples exhibit interesting ionic transport properties, with the PSZO sample demonstrating notable characteristics. It displays higher conductivity at elevated temperatures and good stability in both reducing and oxidizing atmospheres, desirable characteristics for a wide range of technological applications. Furthermore, the PSZO sample shows a rapid reoxidation process, making it a promising material for a wide range of applications, including fuel cells, chemical sensors, and other technological devices focused on clean energy generation and environmental sustainability.

4. Conclusions

This work demonstrated the successful synthesis of single-phase pyrochlore structures through the solvothermal method. The compositions studied were $Pr_2Zr_2O_7$ (PZO), $PrSmZr_2O_7$ (PSZO), and $Sm_2Zr_2O_7$ (SZO). After synthesis, dense ceramics with approximately 96% of relative density were obtained using the Spark Plasma Sintering (SPS) method.

Electrochemical Impedance Spectroscopy (EIS) measurements conducted under argon atmosphere showed that the samples with Pr presented higher total conductivity than SZO. According to the EIS data, the

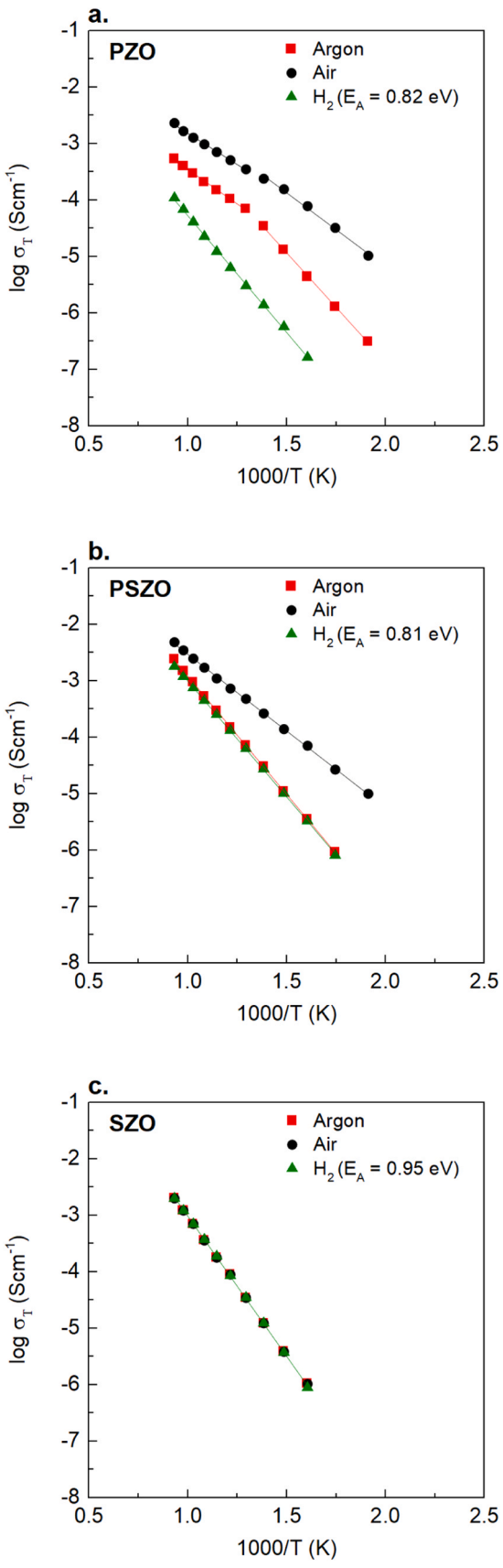

Fig. 8. Arrhenius plot of the overall conductivity in H_2 for (a) SZO, (b) PSZO, and (c) PZO. The conductivities obtained in argon and air are included in each figure. The activation energy (eV), with errors in the range 0.02–0.05 eV, are shown beside each data set.

presence of Sm introduced inhomogeneity, requiring two RC elements associated in series to describe the electrical response of the PSZO and SZO samples. Upon reoxidizing the samples in air, fast reoxidation was observed in the PZO and PSZO samples, leading to increased conductivity due to hole creation on oxygen. PSZO sample presented an evident preferential oxidation process along the grain boundaries.

Comparisons with reference ion-oxide solid electrolyte materials sintered using SPS revealed that the PSZO sample exhibited comparable conductivity with LSGM and GDC at low temperatures and higher conductivity than YSZ across the entire temperature range.

The materials displayed good stability in a reducing (H_2) atmosphere. In this atmosphere, PZO exhibited decreased conductivity due to the reduction of Pr(IV) ions to Pr(III). The PSZO sample showed similar conductivity in both H_2 and argon atmospheres, indicating almost complete reduction of Pr during the SPS process. The SZO sample displayed almost the same conductivity under argon, air, and H_2 atmospheres.

Given their excellent relative density, good conductivity, and rapid oxidation properties, particularly in the case of PSZO, these materials hold promise for applications requiring thermal and physical stability, as well as fast oxidation-reduction processes, such as Solid Oxide Fuel Cells (SOFCs), gas sensors, and other technologies for clean energy applications.

CRediT authorship contribution statement

Emerson Luiz dos Santos Veiga: Conceptualization, Methodology, Validation, Formal analysis, Investigation, Visualization, Writing - Original draft. **Héctor Beltrán-Mir:** Conceptualization, Methodology, Resources, Supervision Writing – review & editing. **Sébastien Fourcade:** Conceptualization, Methodology. **U-Chan Chung:** Conceptualization, Methodology, Resources, Supervision, Writing – review & editing. **Dominique Michau:** Conceptualization, Methodology. **Catherine Elissalde:** Conceptualization, Methodology, Resources, Supervision, Writing – review & editing. **Fabrice Mauvy:** Conceptualization, Methodology, Resources, Supervision, Writing – review & editing. **Eloísa Cordoncillo:** Conceptualization, Methodology, Resources, Supervision, Writing – review & editing.

Declaration of Competing Interest

The authors declare that they have no known competing financial interests or personal relationships that could have appeared to influence the work reported in this paper.

Acknowledgments

H.B-M, E.C., and E.L.S.V. thank the Spanish Ministerio de Ciencia e Innovación [Project PID2020-116149GB-I00] for the financial support. E.L.S.V thanks the Generalitat Valenciana for the predoctoral contract [GRISOLIA/2019/054] and for the financial support for the international stay [CIBEFP/2021/22].

Appendix A. Supporting information

Supplementary data associated with this article can be found in the online version at doi:10.1016/j.jeurceramsoc.2023.12.070.

References

[1] B. Basu, K. Balani, Advanced Structural Ceramics, Wiley, 2011, https://doi.org/10.1002/9781118037300.
[2] J.F. Shackelford, R.H. Doremus, Ceramic and glass materials: structure, Prop. Process. (2008), https://doi.org/10.1007/978-0-387-73362-3.
[3] M.N. Rahaman, Ceramic Processing, CRC Press, 2017, https://doi.org/10.1201/9781315276045.

[4] J. Zhang, S. Ricote, P.V. Hendriksen, Y. Chen, Advanced materials for thin-film solid oxide fuel cells: recent progress and challenges in boosting the device performance at low temperatures, Adv. Funct. Mater. 32 (2022), https://doi.org/10.1002/ADFM.202111205.

[5] J.L. Choi, B.K. Park, S.B. Lee, R.H. Song, J.W. Lee, Efficient and robust ceramic interconnects based on a mixed-cation perovskite for solid oxide fuel cells, Ceram. Int 45 (2019) 4902–4908, https://doi.org/10.1016/J.CERAMINT.2018.11.189.

[6] K. Singh, R. Kannan, V. Thangadurai, Perspective of perovskite-type oxides for proton conducting solid oxide fuel cells, Solid State Ion. 339 (2019) 114951, https://doi.org/10.1016/J.SSI.2019.04.014.

[7] Z. Shao, W. Zhou, Z. Zhu, Advanced synthesis of materials for intermediate-temperature solid oxide fuel cells, Prog. Mater. Sci. 57 (2012) 804–874, https://doi.org/10.1016/J.PMATSCI.2011.08.002.

[8] U. Javed, K.P. Ramaiyan, C.R. Kreller, E.L. Brosha, R. Mukundan, A.V. Morozov, Using sensor arrays to decode NO_x/NH_3/C_3H_8 gas mixtures for automotive exhaust monitoring, Sens Actuators B Chem. 264 (2018) 110–118, https://doi.org/10.1016/J.SNB.2018.02.069.

[9] L. Kulhari, K. Ray, N. Suri, P.K. Khanna, Detection and characterization of CO gas using LTCC micro-hotplates, Sadhana Acad. Proc. Eng. Sci. 45 (2020) 1–6, https://doi.org/10.1007/S12046-020-1316-5/FIGURES/11.

[10] C. Arul, K. Moulaee, N. Donato, D. Iannazzo, N. Lavanya, G. Neri, C. Sekar, Temperature modulated Cu-MOF based gas sensor with dual selectivity to acetone and NO_2 at low operating temperatures, Sens. Actuators B Chem. 329 (2021) 129053, https://doi.org/10.1016/J.SNB.2020.129053.

[11] I. Jaouali, H. Hamrouni, N. Moussa, M.F. Nsib, M.A. Centeno, A. Bonavita, G. Neri, S.G. Leonardi, $LaFeO_3$ ceramics as selective oxygen sensors at mild temperature, Ceram. Int 44 (2018) 4183–4189, https://doi.org/10.1016/J.CERAMINT.2017.11.221.

[12] Y. Shen, X. Zhong, J. Zhang, T. Li, S. Zhao, B. Cui, D. Wei, Y. Zhang, K. Wei, In-situ growth of mesoporous In_2O_3 nanorod arrays on a porous ceramic substrate for ppb-level NO_2 detection at room temperature, Appl. Surf. Sci. 498 (2019) 143873, https://doi.org/10.1016/J.APSUSC.2019.143873.

[13] L. Han, S. Cai, M. Gao, J. Hasegawa, P. Wang, J. Zhang, L. Shi, D. Zhang, Selective catalytic reduction of NO_x with NH_3 by using novel catalysts: state of the art and future prospects, Chem. Rev. 119 (2019) 10916–10976, https://doi.org/10.1021/acs.chemrev.9b00202.

[14] C. He, J. Cheng, X. Zhang, M. Douthwaite, S. Pattisson, Z. Hao, Recent advances in the catalytic oxidation of volatile organic compounds: a review based on pollutant sorts and sources, Chem. Rev. 119 (2019) 4471–4568, https://doi.org/10.1021/acs.chemrev.8b00408.

[15] C. Yang, G. Miao, Y. Pi, Q. Xia, J. Wu, Z. Li, J. Xiao, Abatement of various types of VOCs by adsorption/catalytic oxidation: a review, Chem. Eng. J. 370 (2019) 1128–1153, https://doi.org/10.1016/J.CEJ.2019.03.232.

[16] X.I. Pereira-Hernández, A. DeLaRiva, V. Muravev, D. Kunwar, H. Xiong, B. Sudduth, M. Engelhard, L. Kovarik, E.J.M. Hensen, Y. Wang, A.K. Datye, 2019. Tuning Pt-CeO_2 interactions by high-temperature vapor-phase synthesis for improved reducibility of lattice oxygen, Nature Communications 2019 10:1. 10, pp. 1–10. https://doi.org/10.1038/s41467–019-09308–5.

[17] M.A. Subramanian, G. Aravamudan, G.V. Subba Rao, Oxide pyrochlores — a review, Prog. Solid State Chem. 15 (1983) 55–143, https://doi.org/10.1016/0079-6786(83)90001-8.

[18] G.D. Blundred, C.A. Bridges, M.J. Rosseinsky, New oxidation states and defect chemistry in the pyrochlore structure, Angew. Chem. Int. Ed. 43 (2004) 3562–3565, https://doi.org/10.1002/anie.200453819.

[19] R. Mouta, R.X. Silva, C.W.A. Paschoal, Tolerance factor for pyrochlores and related structures, Acta Crystallogr B Struct. Sci. Cryst. Eng. Mater. 69 (2013) 439–445, https://doi.org/10.1107/S2052519213020514.

[20] N. Mahato, A. Banerjee, A. Gupta, S. Omar, K. Balani, Progress in material selection for solid oxide fuel cell technology: a review, Prog. Mater. Sci. 72 (2015) 141–337, https://doi.org/10.1016/J.PMATSCI.2015.01.001.

[21] J.R. Varcoe, P. Atanassov, D.R. Dekel, A.M. Herring, M.A. Hickner, P.A. Kohl, A. R. Kucernak, W.E. Mustain, K. Nijmeijer, K. Scott, T. Xu, L. Zhuang, Anion-exchange membranes in electrochemical energy systems, Energy Environ. Sci. 7 (2014) 3135–3191, https://doi.org/10.1039/C4EE01303D.

[22] N. Cioateră, E.A. Voinea, C.I. Spînu, Pyrochlores as cathodes in solid oxide fuel cells, Pyrochlore Ceram. Prop. Process. Appl. (2022) 433–448, https://doi.org/10.1016/B978-0-323-90483-4.00013-1.

[23] A.V. Shlyakhtina, K.S. Pigalskiy, Tolerance factor as the basic criterion in searching for promising oxygen-ion and proton conductors among $Ln_{2-x}D_xM_2O_{7-\delta}$ (Ln = La-Lu; M= Sn, Ti, Zr, Hf; D= Sr, Ca, Mg; x = 0, 0.1) 3+/4+ pyrochlores, Mater. Res. Bull. 116 (2019) 72–78, https://doi.org/10.1016/J.MATERRESBULL.2019.04.021.

[24] L. Jiang, Y. Liu, W. Sun, M. Tang, Y. Zhang, S. Lv, J. Wang, Y. Liu, C. Wang, P. Sun, J. Zheng, F. Liu, G. Lu, Mixed potential type sensor based on $Gd_2Zr_2O_7$ solid electrolyte and $BiVO_4$ sensing electrode for effective detection of triethylamine, J. Hazard Mater. 440 (2022), https://doi.org/10.1016/j.jhazmat.2022.129695.

[25] M. Ganesan, V. Jayaraman, P. Selvaraj, K.M. Mani, D.-H. Kim, Pyrochlore cerium stannate ($Ce_2Sn_2O_7$) for highly sensitive NO_2 gas sensing at room temperature, Appl. Surf. Sci. 624 (2023) 157135, https://doi.org/10.1016/j.apsusc.2023.157135.

[26] L. Jiang, C. Wang, J. Wang, F. Liu, R. You, S. Lv, G. Zeng, Z. Yang, J. He, A. Liu, X. Yan, P. Sun, J. Zheng, G. Lu, Pyrochlore Ca-doped $Gd_2Zr_2O_7$ solid state electrolyte type sensor coupled with ZnO sensing electrode for sensitive detection of HCHO, Sens Actuators B Chem. 309 (2020) 127768, https://doi.org/10.1016/j.snb.2020.127768.

[27] D.A. Kuznetsov, M.A. Naeem, P.V. Kumar, P.M. Abdala, A. Fedorov, C.R. Müller, Tailoring lattice oxygen binding in ruthenium pyrochlores to enhance oxygen evolution activity, J. Am. Chem. Soc. 142 (2020) 7883–7888, https://doi.org/10.1021/jacs.0c01135.

[28] S. Sun, Y. Xue, D. Yang, Z. Pei, L. Fang, Y. Xia, R. Ti, C. Wang, C. Liu, B. Xiong, Z. Fu, X. Yin, Bismuth pyrochlores with varying Fe/Co ratio for efficient Multi-functional catalysis: structure evolution versus photo- and electro-catalytic activities, Chem. Eng. J. 448 (2022) 137580, https://doi.org/10.1016/j.cej.2022.137580.

[29] D. Jain, S. Saha, Spectroscopic and kinetic insights into the methane reforming over Ce-pyrochlores, Mol. Catal. 492 (2020) 110964, https://doi.org/10.1016/j.mcat.2020.110964.

[30] J. Deng, S. Li, X. Yin, M. Li, J. Wang, Y. Chen, Y. Chen, Influence of surface Ce/Zr ratio on formation of κ-$Ce_2Zr_2O_8$ superstructure and its application in three-way catalysis, J. Rare Earths 41 (2023) 67–76, https://doi.org/10.1016/j.jre.2021.12.005.

[31] E.L. dos Santos Veiga, X.V. Villafruela, J. Llorca, H. Beltrán-Mir, E. Cordoncillo, The catalytic activity of the $Pr_2Zr_{2-x}Fe_xO_{7\pm\delta}$ system for the CO oxidation reaction, J. Am. Ceram. Soc. (2022), https://doi.org/10.1111/jace.18846.

[32] G. Lan, B. Ouyang, J. Song, The role of low-lying optical phonons in lattice thermal conductance of rare-earth pyrochlores: a first-principle study, Acta Mater. 91 (2015) 304–317, https://doi.org/10.1016/j.actamat.2015.03.004.

[33] Y. Fan, Q. Wu, Y. Yao, J. Wang, J. Zhao, B. Liu, Temperature effect on mechanical and thermal properties of multicomponent rare-earth zirconate pyrochlores, J. Am. Ceram. Soc. 106 (2023) 1500–1512, https://doi.org/10.1111/jace.18816.

[34] L. Gao, K. Liang, Z. Guan, Z. Liu, Z. Fang, H. Chen, J. Zhang, Disordered structures and dielectric properties of Ni-doped bismuth magnesium niobate pyrochlores, J. Phys. Chem. C 125 (2021) 27793–27799, https://doi.org/10.1021/acs.jpcc.1c08515.

[35] K. Liang, L. Gao, Z. Fang, Z. Liu, Z. Guan, H. Chen, J. Zhang, Effects of Ni^{2+} substitution on the structure and dielectric properties of $Bi_{1.5}MgNb_{1.5}O_7$ cubic pyrochlores, J. Eur. Ceram. Soc. 41 (2021) 3425–3431, https://doi.org/10.1016/j.jeurceramsoc.2020.10.030.

[36] J.A. Díaz-Guillén, A.F. Fuentes, M.R. Díaz-Guillén, J.M. Almanza, J. Santamaría, C. León, The effect of homovalent a-site substitutions on the ionic conductivity of pyrochlore-type $Gd_2Zr_2O_7$, J. Power Sources 186 (2009) 349–352, https://doi.org/10.1016/j.jpowsour.2008.09.106.

[37] A.V. Shlyakhtina, S.N. Savvin, A.V. Levchenko, A.V. Knotko, P. Fedtke, A. Busch, T. Barfels, M. Wienecke, L.G. Shcherbakova, Study of bulk and grain-boundary conductivity of $Ln_{2+x}Hf_{2-x}O_{7-\delta}$ (Ln = Sm-Gd; x = 0, 0.096) pyrochlores, J. Electroceram. 24 (2010) 300–307, https://doi.org/10.1007/s10832-009-9572-0.

[38] J.K. Gill, O.P. Pandey, K. Singh, Ionic conductivity, structural and thermal properties of pure and Sr^{2+} doped $Y_2Ti_2O_7$ pyrochlores for SOFC, Solid State Sci. 13 (2011) 1960–1966, https://doi.org/10.1016/j.solidstatesciences.2011.08.025.

[39] E.L. dos S. Veiga, M. Fortuño-Morte, H. Beltrán-Mir, E. Cordoncillo, Effect of the oxidation states on the electrical properties of Fe-doped $Pr_2Zr_2O_7$ pyrochlore, J. Mater. Res. Technol. 16 (2022) 201–215, https://doi.org/10.1016/j.jmrt.2021.11.146.

[40] M. Cologna, B. Rashkova, R. Raj, Flash sintering of nanograin zirconia in <5 s at 850°C, J. Am. Ceram. Soc. 93 (2010) 3556–3559, https://doi.org/10.1111/j.1551-2916.2010.04089.x.

[41] H. Guo, A. Baker, J. Guo, C.A. Randall, Cold sintering process: a novel technique for low-temperature ceramic processing of ferroelectrics, J. Am. Ceram. Soc. 99 (2016) 3489–3507, https://doi.org/10.1111/jace.14554.

[42] Z.A. Munir, U. Anselmi-Tamburini, M. Ohyanagi, The effect of electric field and pressure on the synthesis and consolidation of materials: a review of the spark plasma sintering method, J. Mater. Sci. 41 (2006) 763–777, https://doi.org/10.1007/s10853-006-6555-2.

[43] B.N. Ezealigo, R. Orrù, C. Elissalde, H. Debéda, U.-C. Chung, M. Maglione, G. Cao, Influence of the spark plasma sintering temperature on the structure and dielectric properties of $BaTi_{(1-x)}Zr_xO_3$ ceramics, Ceram. Int. 47 (2021) 3614–3625, https://doi.org/10.1016/j.ceramint.2020.09.210.

[44] M. Legallais, S. Fourcade, U.-C. Chung, D. Michau, M. Maglione, F. Mauvy, C. Elissalde, Fast re-oxidation kinetics and conduction pathway in spark plasma sintered ferroelectric ceramics, J. Eur. Ceram. Soc. 38 (2018) 543–550, https://doi.org/10.1016/j.jeurceramsoc.2017.07.026.

[45] Z.-H. Zhang, Z.-F. Liu, J.-F. Lu, X.-B. Shen, F.-C. Wang, Y.-D. Wang, The sintering mechanism in spark plasma sintering – proof of the occurrence of spark discharge, Scr. Mater. 81 (2014) 56–59, https://doi.org/10.1016/j.scriptamat.2014.03.011.

[46] B. Liu, Y. Zhang, $La_{0.9}Sr_{0.1}Ga_{0.8}Mg_{0.2}O_{3-\delta}$ sintered by spark plasma sintering (SPS) for intermediate temperature SOFC electrolyte, J. Alloy. Compd. 458 (2008) 383–389, https://doi.org/10.1016/J.JALLCOM.2007.03.126.

[47] B.H. Toby, R.B. Von Dreele, GSAS-II: the genesis of a modern open-source all purpose crystallography software package, J. Appl. Crystallogr. 46 (2013) 544–549, https://doi.org/10.1107/S0021889813003531.

[48] Blake G.R., Hartge K.H., 2018. Bulk density. https://doi.org/10.2136/sssabookser5.1.2ed.c13.

[49] A.P. Anantharaman, H.P. Dasari, Potential of pyrochlore structure materials in solid oxide fuel cell applications, Ceram. Int. 47 (2021) 4367–4388, https://doi.org/10.1016/j.ceramint.2020.10.012.

[50] B.P. Mandal, N. Garg, S.M. Sharma, A.K. Tyagi, Preparation, XRD and Raman spectroscopic studies on new compounds $RE_2Hf_2O_7$ (RE=Dy, Ho, Er, Tm, Lu, Y): pyrochlores or defect-fluorite? J. Solid State Chem. 179 (2006) 1990–1994, https://doi.org/10.1016/j.jssc.2006.03.036.

[51] R.D. Shannon, Revised effective ionic radii and systematic studies of interatomic distances in halides and chalcogenides, Acta Crystallogr. Sect. A 32 (1976) 751–767, https://doi.org/10.1107/S0567739476001551.

[52] D.K. Smith, J. Fiala, E. Ryba, The Rietveld Method, Oxford University Press, N. Y. (1993), https://doi.org/10.1017/S0885715600019497.
[53] B.H. Toby, R factors in Rietveld analysis: how good is good enough? Powder Diffr. 21 (2006) 67–70, https://doi.org/10.1154/1.2179804.
[54] R. Ubic, I. Abrahams, Y. Hu, Oxide ion disorder in $Nd_2Hf_2O_7$, J. Am. Ceram. Soc. 91 (2007) 235–239, https://doi.org/10.1111/j.1551-2916.2007.02025.x.
[55] S. Kramer, M. Spears, H.L. Tuller, Conduction in titanate pyrochlores: role of dopants, Solid State Ion. 72 (1994) 59–66, https://doi.org/10.1016/0167-2738(94)90125-2.
[56] A.G. Krasnov, I.V. Piir, M.S. Koroleva, N.A. Sekushin, Y.I. Ryabkov, M. M. Piskaykina, V.A. Sadykov, E.M. Sadovskaya, V.V. Pelipenko, N.F. Eremeev, The conductivity and ionic transport of doped bismuth titanate pyrochlore $Bi_{1.6}M_xTi_2O_{7-\delta}$ (M – Mg, Sc, Cu), Solid State Ion.-. 302 (2017) 118–125, https://doi.org/10.1016/j.ssi.2016.12.019.
[57] X. Vendrell, A.R. West, Electrical properties of yttria-stabilized zirconia, YSZ single crystal: local AC and long range DC conduction, J. Electrochem. Soc. 165 (2018) F966–F975, https://doi.org/10.1149/2.0881811jes.
[58] M. Jovaní, H. Beltrán-Mir, E. Cordoncillo, A.R. West, Atmosphere- and voltage-dependent electronic conductivity of oxide-ion-conducting $Zr_{1-x}Y_xO_{2-x/2}$ ceramics, Inorg. Chem. 56 (2017) 7081–7088, https://doi.org/10.1021/acs.inorgchem.7b00673.
[59] X. Vendrell, A.R. West, Induced *p*-type semiconductivity in yttria-stabilized zirconia, J. Am. Ceram. Soc. 102 (2019) 6100–6106, https://doi.org/10.1111/jace.16492.
[60] M. Jovaní, H. Beltrán-Mir, E. Cordoncillo, A.R. West, Field-induced p-n transition in yttria-stabilized zirconia, Sci. Rep. 9 (2019) 18538, https://doi.org/10.1038/s41598-019-54588-y.
[61] O. Bezdorozhev, H. Borodianska, Y. Sakka, O. Vasylkiv, Spark plasma sintered Ni-YSZ/YSZ Bi-layers for solid oxide fuel cell, J. Nanosci. Nanotechnol. 13 (2013) 4150–4157, https://doi.org/10.1166/jnn.2013.7213.
[62] A. Kabir, S. Santucci, N. Van Nong, M. Varenik, I. Lubomirsky, R. Nigon, P. Muralt, V. Esposito, Effect of oxygen defects blocking barriers on gadolinium doped ceria (GDC) electro-chemo-mechanical properties, Acta Mater. 174 (2019) 53–60, https://doi.org/10.1016/J.ACTAMAT.2019.05.009.